

# Auxiliary Material

Subduction of oceanic asthenosphere: evidence from sub-slab seismic anisotropy

Teh-Ru Alex Song, Hitoshi Kawakatsu

correspondence to: [tehrusong@gmail.com](mailto:tehrusong@gmail.com)

## 1. The effect of anisotropy in the subducting slab

Here we briefly discuss the effect of anisotropy in the subducting slab to shear-wave splitting measurements. Surface wave tomography indicates frozen-in azimuthal anisotropy in the shallow oceanic upper mantle, or oceanic lithosphere [Smith *et al.*, 2004; Debayle *et al.*, 2005; Maggi *et al.*, 2006]. If the thickness of frozen-in azimuthal anisotropy within the incoming plate is 30 km or less, it has very limited impact on sub-slab SKS fast splitting direction because of low sensitivity of long period wave (8-15 seconds) on thin anisotropic layer. Recent analysis on anisotropy in the subducted slab beneath Mexico also suggests a strong but localized anisotropic layer in the topmost 5 km of the subducted oceanic mantle [Song and Kim, 2012]. If this is the case, shear-wave splitting patterns predicted by the entrainment of oceanic asthenosphere remain largely unchanged. As discussed by Long and Silver [2008; 2009], the trench-parallel (or sub-parallel) fast splitting direction observed in many subduction zones is not consistent with the orientation of the fossil spreading direction, which also argues against the dominant role of slab anisotropy on shear wave splitting patterns in subduction zones. Most importantly, the effect of radial anisotropy dominates the splitting behavior for steep subduction zones and the direction of fast axis appears only relevant for shallow subduction zones (Figure 2, Figure S3).

## 2. Calculations of phase velocity for quasi-S waves upon azimuthal anisotropy, radial anisotropy and orthorhombic anisotropy symmetry

The elastic stiffness tensor  $c_{ijkl}$  can be denoted as  $c_{ij}$  using notations,

$$\begin{aligned} ij &= i \\ kl &= j \\ c_{ijkl} &= c_{ij} \end{aligned} \quad (1)$$

. The elastic tensor  $c_{ij}$  can be expressed as

$$c_{ij} = \begin{bmatrix} c_{11} & c_{12} & c_{13} & & & \\ c_{21} & c_{22} & c_{23} & & & \\ c_{31} & c_{32} & c_{33} & & & \\ & & & c_{44} & & \\ & & & & c_{55} & \\ & & & & & c_{66} \end{bmatrix} \quad (2)$$

for anisotropic media with a general orthorhombic anisotropy symmetry. There are 9 independent elastic constants,  $c_{11}$ ,  $c_{22}$ ,  $c_{33}$ ,  $c_{44}$ ,  $c_{55}$ ,  $c_{66}$ ,  $c_{12}$ ,  $c_{13}$  and  $c_{23}$ , while  $c_{12}=c_{21}$ ,  $c_{13}=c_{31}$ ,  $c_{23}=c_{32}$ . The diagonal term can be directly related to P wave and S wave velocity propagating along the symmetry axis. The off-diagonal terms such as  $c_{13}$  and  $c_{23}$  may be related to  $c_{11}$ ,  $c_{22}$ ,  $c_{33}$ ,  $c_{44}$ ,  $c_{55}$  and  $c_{66}$  through the non-dimensional parameter  $\eta$  to form a 7-parameter ‘‘orthorhombic’’ system,

$$\begin{aligned}
c_{13} &= \eta \times [c_{11} - 2 \times c_{55}] \\
c_{23} &= \eta \times [c_{22} - 2 \times c_{44}] \\
c_{12} &= [(c_{11} + c_{22})/2 - 2 \times c_{66}]
\end{aligned} \tag{3}$$

Following *Montanger and Nataf* [1986], the azimuthally averaged effective radial anisotropy of this orthorhombic anisotropic medium can be computed through the following simple relationships:

$$\begin{aligned}
A &= \frac{3}{8}(c_{11} + c_{22}) + \frac{1}{4}c_{12} + \frac{1}{2}c_{66} = \frac{1}{2}(c_{11} + c_{22}) \\
C &= c_{33} \\
F &= \frac{1}{2}(c_{13} + c_{23}) = \eta(A - 2L) \\
L &= \frac{1}{2}(c_{44} + c_{55}) \\
N &= \frac{1}{8}(c_{11} + c_{22}) - \frac{1}{4}c_{12} + \frac{1}{2}c_{66} = c_{66} \\
\eta_{eff} &= \frac{F}{A - 2L}
\end{aligned} \tag{4}$$

where the definition of the radial anisotropy parameters,  $A$ ,  $C$ ,  $F$ ,  $L$ ,  $N$ , follows that of Love. The second equality for  $A$  and  $N$  can be derived by substituting  $C_{12}$  in equation (3) to equation (4). With this definition for the 7-paramter orthorhombic symmetry,  $\eta$  becomes equivalent to that for the azimuthally averaged effective radially anisotropic medium  $\eta_{eff}$ .

For this medium, the strength of radial and azimuthal anisotropy may be defined as follows

$$\begin{aligned}
R_s &= \sqrt{\frac{N}{L}} - 1 \\
R_p &= \sqrt{\frac{A}{C}} - 1 \\
A_s &= \sqrt{\frac{c_{55}}{c_{44}}} - 1 \\
A_p &= \sqrt{\frac{c_{11}}{c_{22}}} - 1
\end{aligned} \tag{5}$$

where,  $R_s$  and  $R_p$  refer to effective S wave and P wave radial anisotropy and  $A_s$  and  $A_p$  refer to S wave and P wave azimuthal anisotropy, respectively. The starting elastic constant of isotropic medium is set with P wave velocity of 8.045 km/s, S wave velocity of 4.485 km/s and density of 3.345 g/cm<sup>3</sup>. In the case of azimuthal anisotropy shown in Figure 1a and Figure S1a,  $R_p$  and  $R_s$  are first set to -2% (a fast vertical symmetry axis along the  $x_3$  direction) and the elastic tensor  $c_{ij}$  is rotated 90° with respect to the  $x_2$  axis so that the rotated tensor  $c_{ij}'$  has a fast symmetry axis along the  $x_1$  direction. . In the case of radial anisotropy shown in Figure 1b and Figure S1b,  $A_p$  and  $A_s$  are set to zero and  $R_p$  and  $R_s$  are set to 4% and 3%, respectively.

To calculate phase velocities for the quasi-P wave, two S waves of all incident angles and back azimuth in a general anisotropic medium, we solve the Christoffel equation,

$$\det|c_{ijkl}n_jn_l - \rho v_n^2 \delta_{ik}| = 0, \quad (5)$$

where  $n_j$  is the unit vector of the wavefront normal and  $v_n$  is the phase velocity normal to the wavefront;  $\rho$  is the density and  $\delta_{ik}$  is the Kronecker delta. The three eigenvalues  $V_p$ ,  $V_{s1}$  and  $V_{s2}$  are phase velocities of the quasi-P wave, two quasi-S waves, respectively. The polarization directions of these waves are the three eigenvectors and they are not necessarily normal or parallel to the wavefront.

### 3. Synthetic SKS splitting in a dipping layer and estimation on the thickness of subducted asthenosphere

Phase velocities of split S waves and splitting pattern shown in Figure 2 are calculated with a tilted symmetry axis in a flat-layer geometry. To take into account the effect of dipping layer geometry on synthetic splitting time, we calculate synthetic waveform following the ray method developed by *Frederiksen and Bostock* [2000] and compute SKS splitting times and fast splitting directions for various slab dips using the cross correlation method [*Ando et al.*, 1983]. Azimuthal anisotropy of 2%, P wave radial anisotropy of 4%, S wave anisotropy of 3% and  $\eta$  of 0.95 used in this calculation is the same as parameters used in Figure 1c. The average splitting time and standard deviation shown in Figure 3 is computed by averaging splitting times assuming a complete back-azimuth sampling of the sub-slab mantle using an incident angle of 12.5°. The synthetic standard deviations reflect the effect of ray backazimuth on splitting times (Figure S4). While most SKS splitting measurements are probably limited in backazimuth, our goal is to provide a first-order estimate on the thickness of asthenosphere entrainment. Given the uncertainties of sub-slab SKS splitting times compiled in global subduction zones, we estimate the thickness of asthenosphere entrainment within data uncertainties and synthetic standard deviations.

In general, the bias in mean splitting time due to the assumption of trench-normal motion of the incoming plate is around 10% for most subduction zones with obliquity of less than 30 degrees, which is not significant compared to the uncertainty in the global dataset [*Long and Silver*, 2009]. While the mean splitting time of real data in each subduction zone is estimated from measurements with an uneven back-azimuth coverage, the predicted mean splitting time shown in Figure 3 is calculated with an uniform back-azimuth coverage. This could lead to a bias in the estimates, but such a potential bias is well inside the calculated standard deviation that contains information on azimuth-dependent splitting time (Figure S5).

### 4. The obliquity of the incoming plate motion and shear wave splitting pattern

For simplicity, we have assumed in the main text and Figure 2 that the motion of the incoming plate is normal to the trench (or parallel to the  $x_1$  axis) and so is the fast

symmetry axis of asthenosphere anisotropy. However, when the motion of incoming plate is oblique to the trench, the fast symmetry axis in the oceanic asthenosphere likely follows the plate motion direction and is no longer parallel to the dipping direction (or  $x_1$  axis). To consider these instances, we first rotate the elastic tensor with respect to the vertical axis (or  $x_3$  axis) according to the obliquity angle  $\alpha$  and subsequently rotate it with respect to the trench axis (or  $x_2$  axis) by the slab dip  $\delta$  before solving the Christoffel equation.

In the cases of shallow subduction zones, we find that the SKS splitting pattern is rotated with respect to the incoming plate motion direction (Figure S3b, S3d). However, in the cases of steep subduction zones, the SKS fast direction is dominated by the effect of strong radial anisotropy through the slab dip and it remains parallel or sub-parallel to the trench (Figure S3c, S3e). These calculations reinforce the conclusion that asthenosphere subduction could explain overall sub-slab fast splitting directions compiled for global subduction zones [Long and Silver, 2008, 2009]. However, for teleseismic S wave splitting ( $20^\circ < \theta < 40^\circ$ ), the predicted fast splitting direction reveals strong azimuthal dependence and it is more affected by the obliquity of plate motion. Interpretations for these splitting measurements warrant greater details that take into account local slab geometry, obliquity of the incoming plate motion to the trench and the direction of the incoming wave.

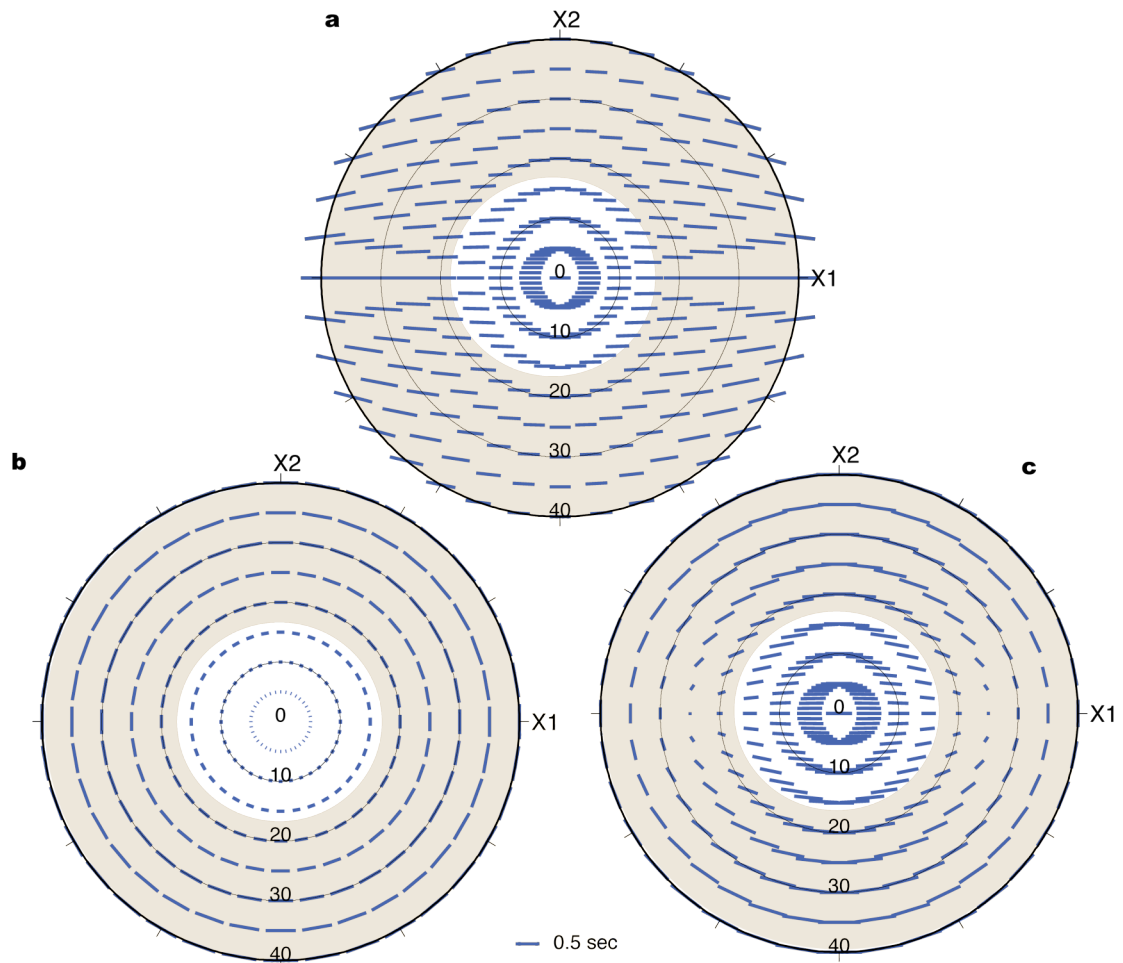


**Figure S1**

Stereo-plots displaying fast polarization directions between incident angles of  $0^\circ$  and  $40^\circ$  for **a.** azimuthal anisotropy, **b.** radial anisotropy and **c.** orthorhombic anisotropy. In **a**, the fast symmetry axis is horizontal along the  $x_1$  axis (see also Figure 1a). In **b**, the slow symmetry axis is vertical along the  $x_3$  axis (see also Figure 1b). In **c**, the directions of symmetry axes can be referred to Figure 1c. Incident angles of the SKS wave and the S wave are shown in white and light brown regime, respectively. The length of each blue bar is scaled with splitting time, assuming a 100 km anisotropic layer.

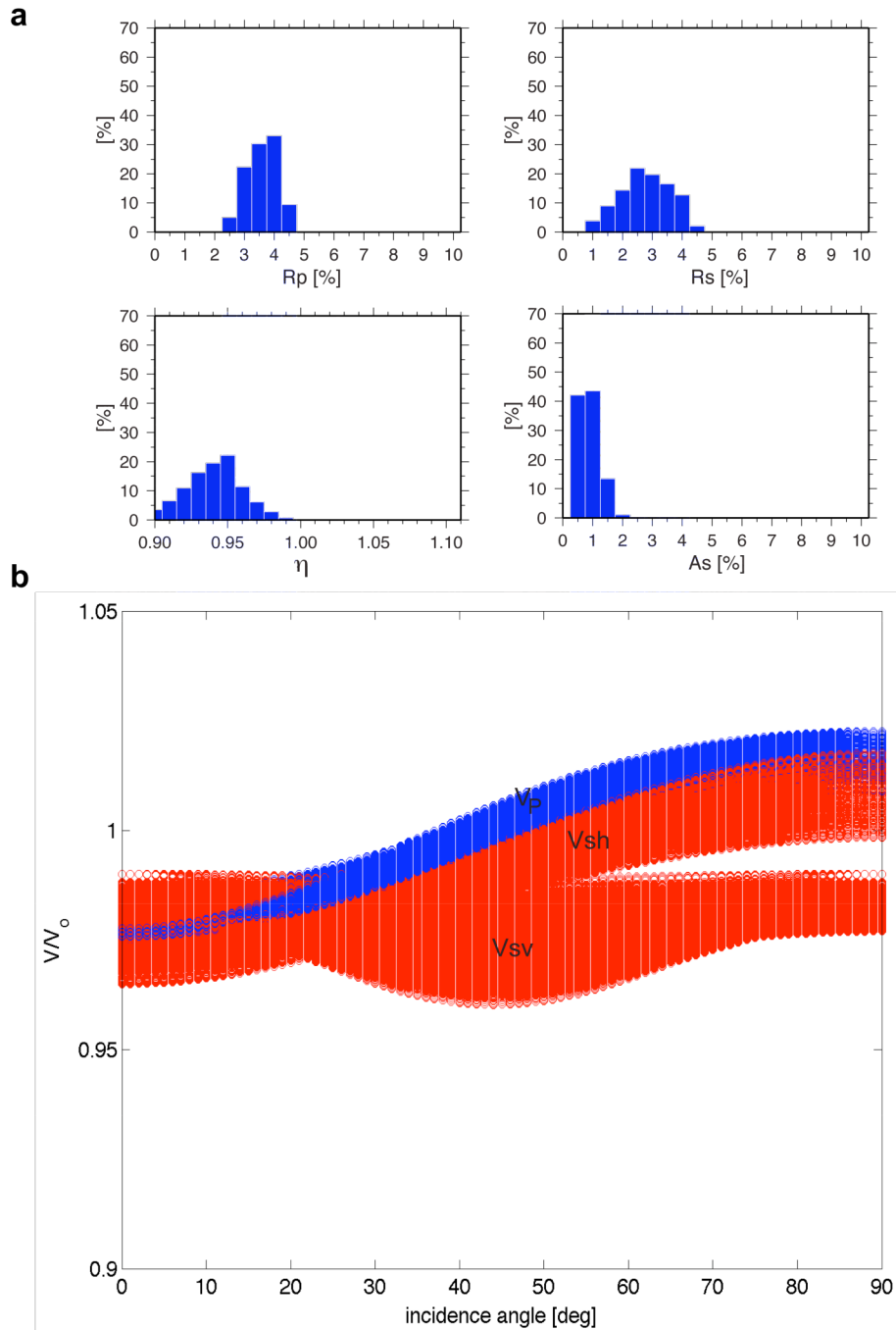


**Figure S2**

A grid search is performed to explore the ranges of effective P wave radial anisotropy ( $R_p$ ), S wave radial anisotropy ( $R_s$ ), S wave azimuthal anisotropy ( $A_s$ ) and  $\eta$  that reproduce orthorhombic anisotropy symmetry and incident angle dependence of phase velocity similar to Figure 1c. Note P wave azimuthal anisotropy is set equal to S wave azimuthal anisotropy for the grid search. **a.** Percentage histograms display the range of parameters among the parameter space that produce point singularities at about  $23 \pm 3$  degrees incident angle, as shown in **b.** Phase velocities,  $V_p$ ,  $V_{sh}$  and  $V_{sv}$  propagating along the  $x_1$  direction are normalized with respect to the reference isotropic velocity,  $V_0$ .

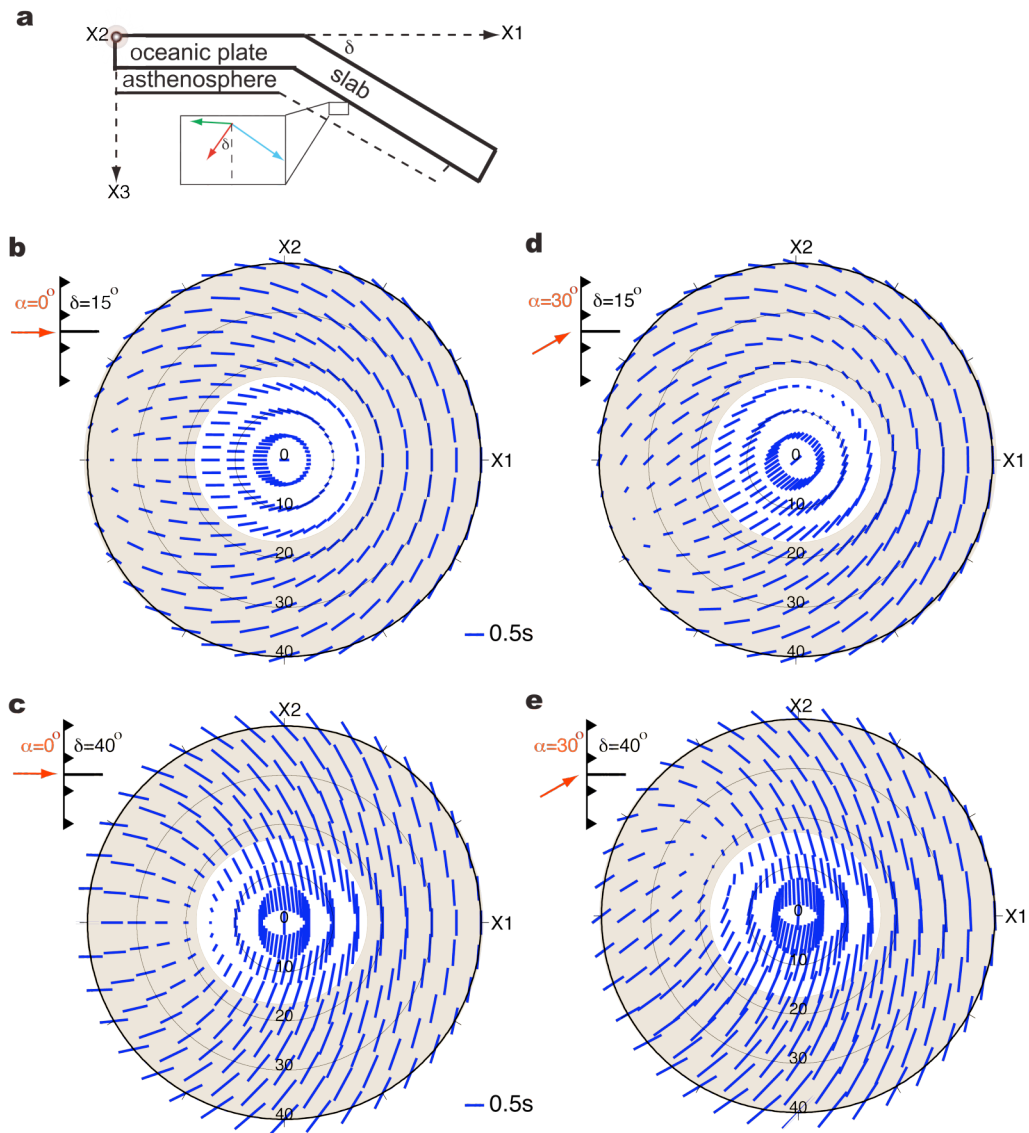


**Figure S3**

Stereo plots of fast polarization directions upon asthenosphere anisotropy symmetry and slab dip. **a.** display the model geometry in the subducted oceanic asthenosphere. The  $x_1$  and  $x_2$  axis are respectively set normal and parallel to the presumed trench axis, while the tilted fast and slow symmetry axes are aligned parallel and normal to the slab dip direction, respectively. **b** and **c** display fast polarization directions predicted for a slab dip  $\delta = 15^\circ$  and  $\delta=40^\circ$ , respectively, assuming that the motion of the incoming plate is normal to the trench, or obliquity  $\alpha=0^\circ$ . The fast polarization direction is calculated every 5 and 10 degrees in incident angle and back azimuth, respectively. Incident angles of the SKS wave and the S wave are shown in white and light brown regime, respectively. **d** and **e** display results for a slab dip  $\delta=15^\circ$  and  $\delta=40^\circ$ , respectively, assuming obliquity  $\alpha=30^\circ$ .

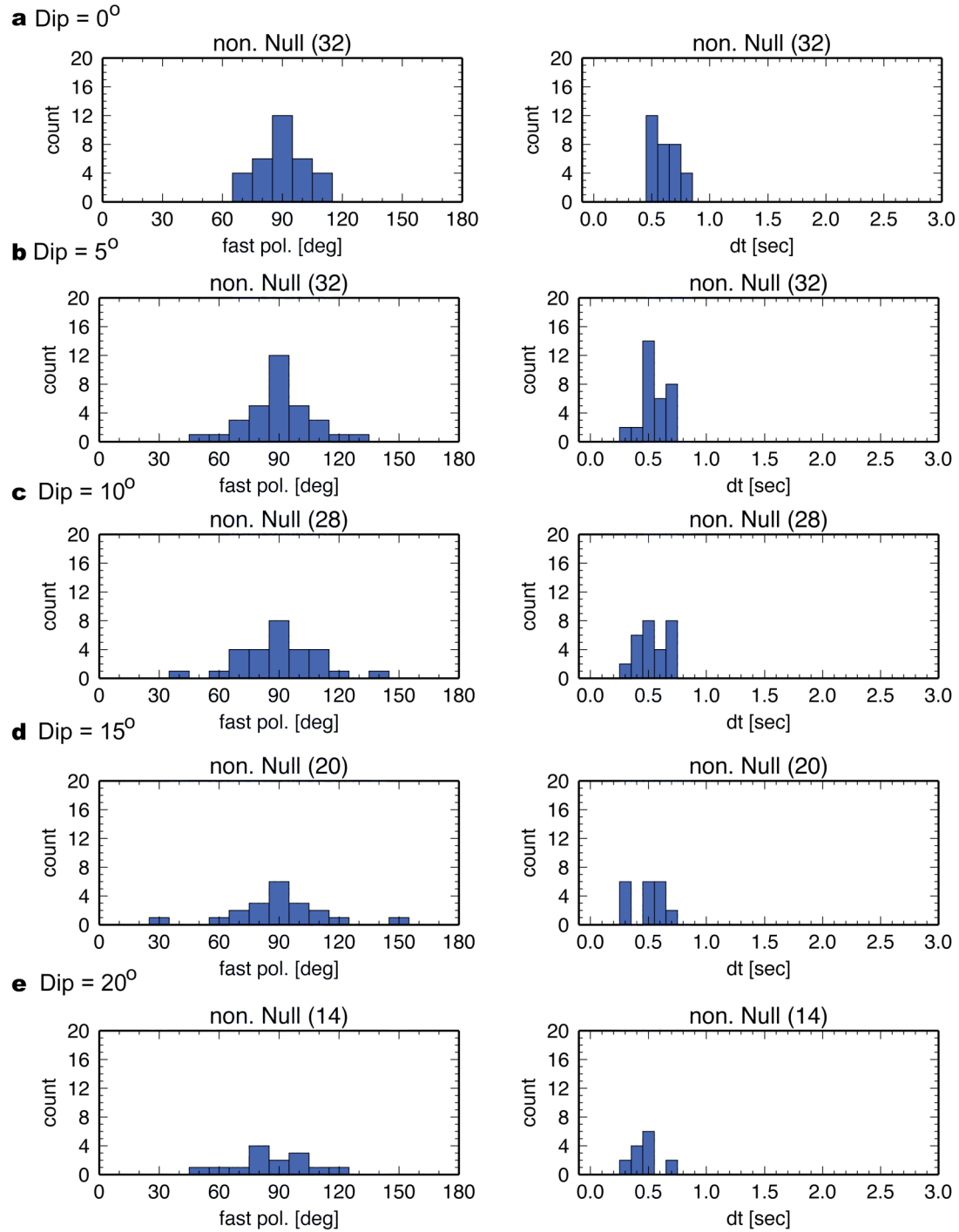


**Figure S4**

Histograms of fast polarization direction and splitting time predicted for a 100 km asthenosphere entrainment for various slab dips shown in **a** to **n**. The subducted asthenosphere has an orthorhombic symmetry with P wave radial anisotropy of 4%, S wave anisotropy of 3%, azimuthal anisotropy of 2% and  $\eta$  of 0.95. The symmetry axis is rotated  $\delta$  degrees clockwise with respect to the  $x_2$  axis (see also Figure 2c for model geometry), where  $\delta$  is the slab dip. The synthetic splitting measurements for an incident angle of  $12.5^\circ$  were done at  $10^\circ$  back azimuth interval and only the non-null measurements ( $\delta t > 0.3$  s) are included in the plot. Fast polarization direction of 90 degree is trench-normal while fast polarization direction of 0 (or 180) degree is trench-parallel.

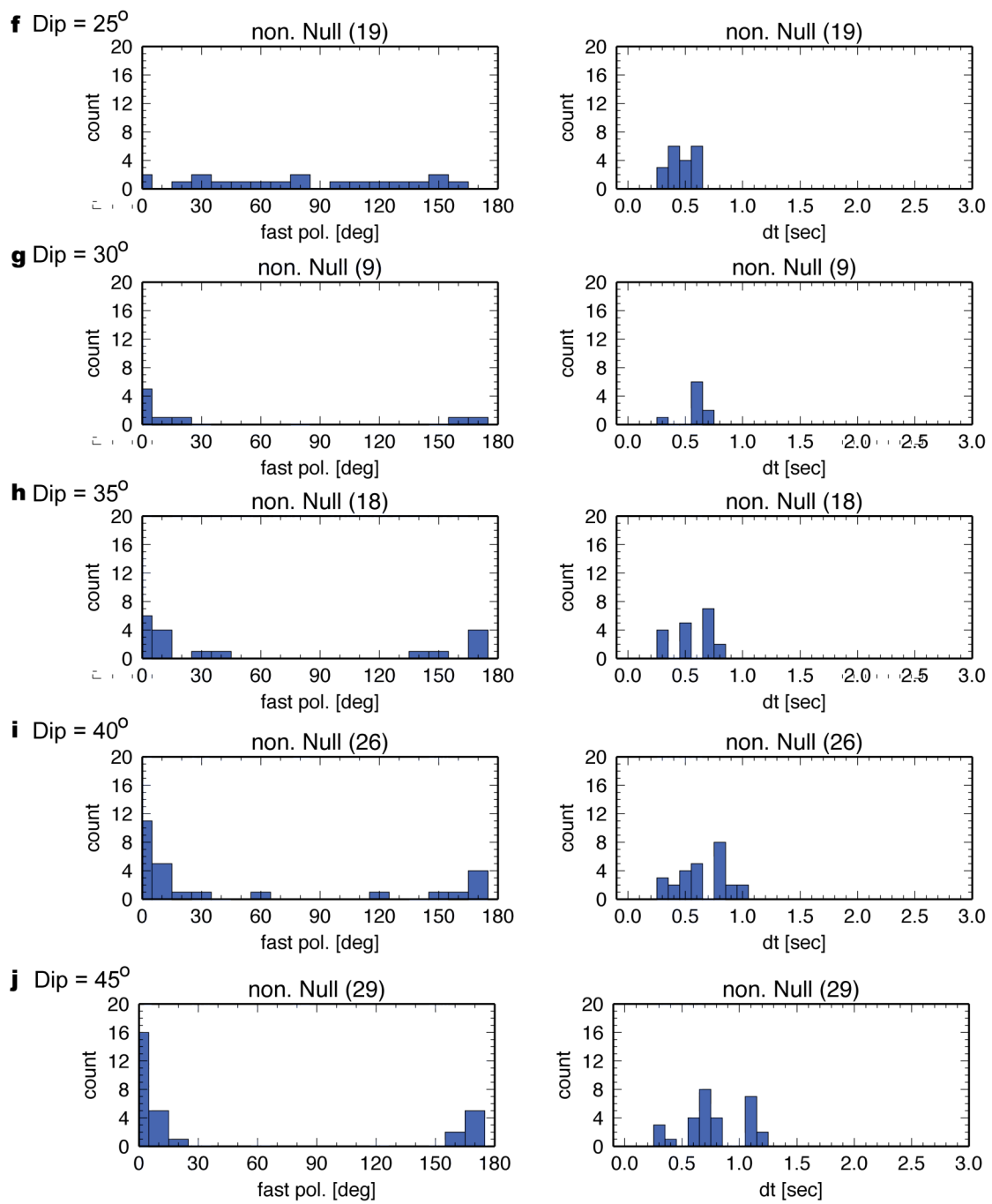


**Figure S4 (cont.)**

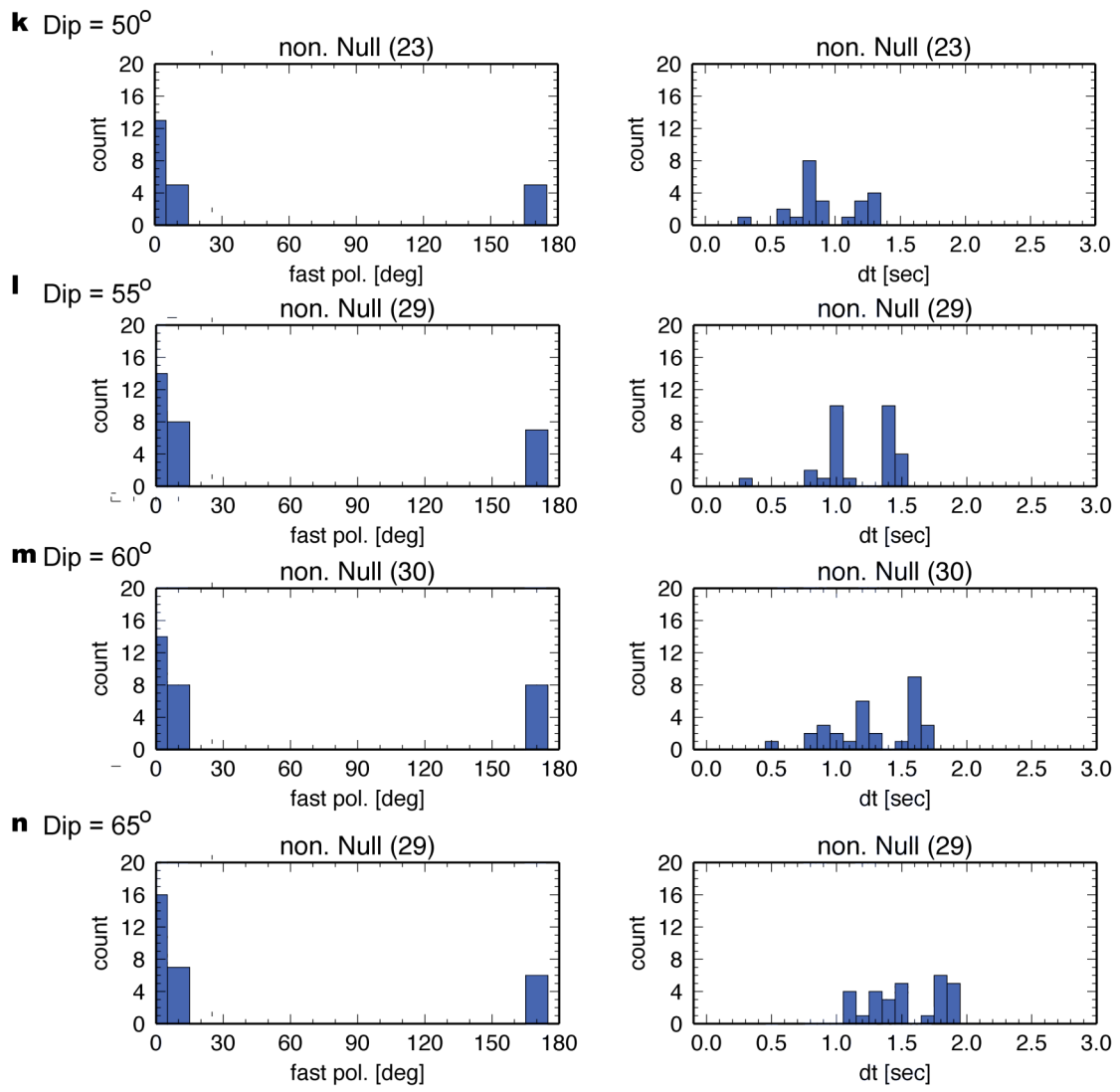


**Figure S4 (cont.)**

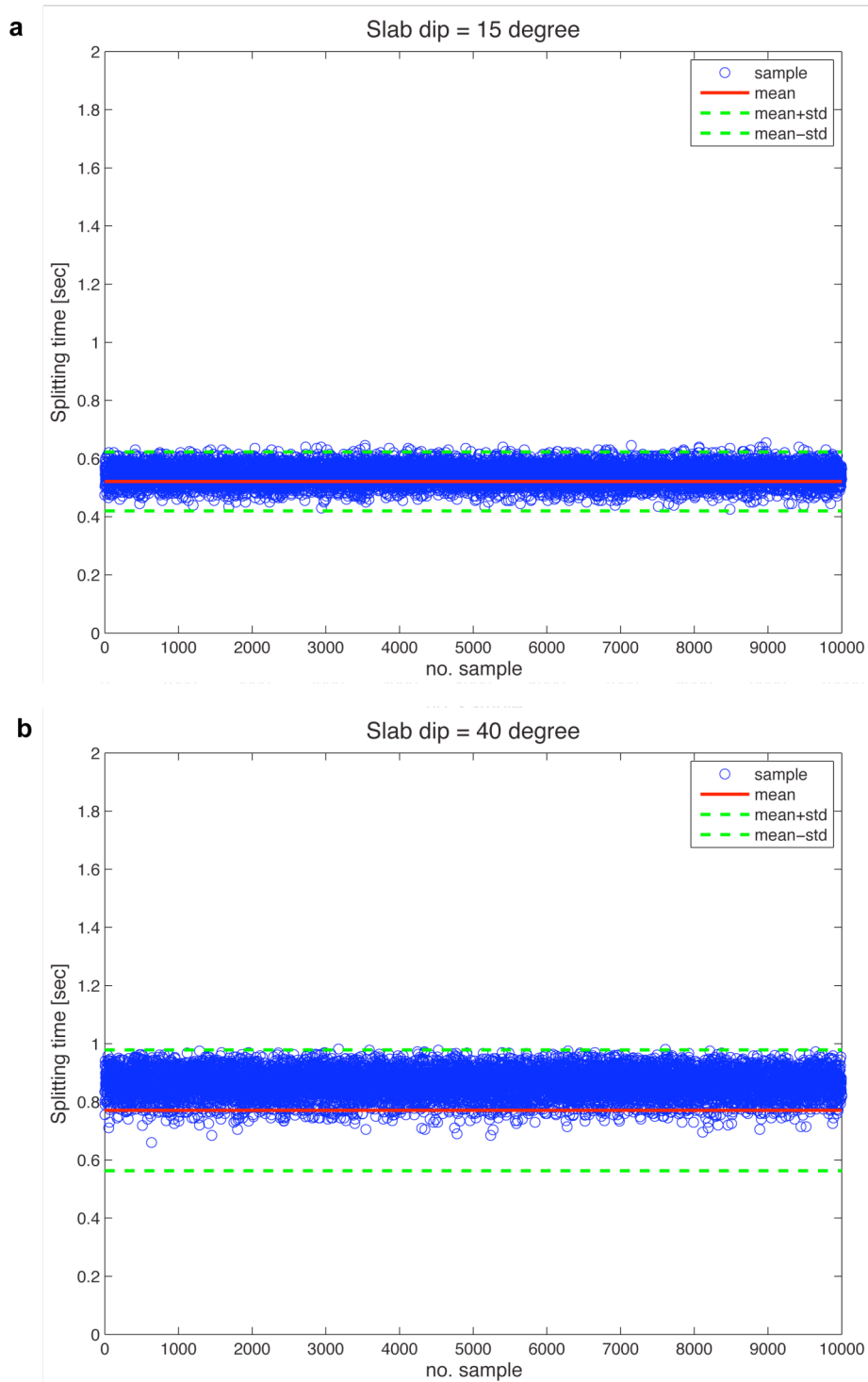


**Figure S5**

Bias of splitting time due to obliquity  $\alpha = 30^\circ$  and uneven ray backazimuth for **a.** slab dip  $\delta = 15^\circ$  and **b.** slab dip  $\delta = 40^\circ$ . We randomly select splitting time measurements from different backazimuth (10 out of 36) and compute mean splitting time over 10000 times (blue circle). The mean splitting time and standard deviation computed with obliquity  $\alpha = 0^\circ$  and even ray backazimuth are shown in red line and green dashed line, respectively. The result indicates that the assumptions of plate motion direction and even ray coverage do not introduce significant bias to the calculation of mean splitting time and the estimate of subduction thickness.

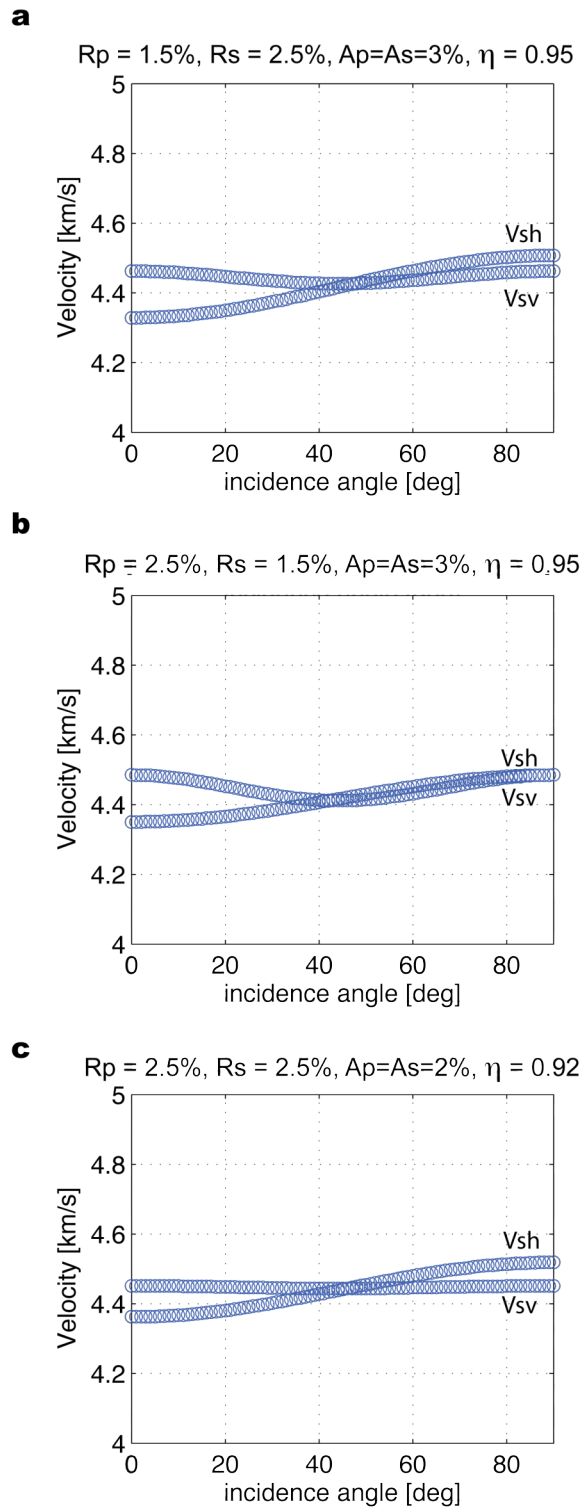


**Figure S6**

Phase velocity of SH and SV wave. In **a**, **b** and **c**, the incoming wave direction is parallel to the  $x_1$  axis. The point singularity is located at about 45-50 incident angle because of relatively low radial anisotropy/azimuthal anisotropy ratio or/and lower  $\eta$ . Off Ryukyu subduction zone, lower radial/azimuthal anisotropy ratio relative to the global average is observed beneath northwestern Philippine Sea plate [Isse et al., 2010]. **d-f** and **g-i** display predicted fast splitting directions for cases **a-c** at a slab dip of  $15^\circ$  and  $40^\circ$ , respectively. The blue bar is not scaled with the splitting time to better visualize variations in fast splitting directions among difference cases.

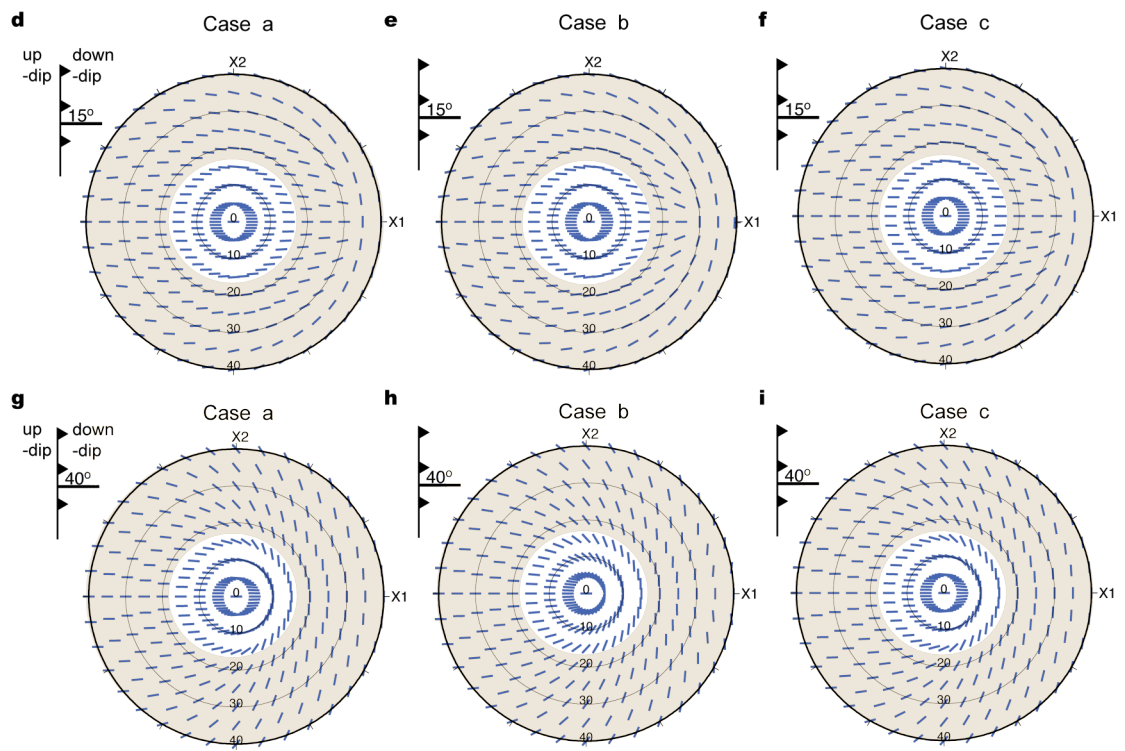


**Figure S6 (cont.)**

Table S1: Nine independent elastic constants for orthorhombic anisotropy used to calculate Figure 1c.

C11	227.34
C22	218.34
C33	205.91
C44	63.33
C55	65.95
C66	68.64
C12	85.57
C13	90.68
C23	87.09

\*The unit for elastic constants is GPa. The isotropic P velocity, S velocity and density are 8045 m/s, 4485 m/s and 3345 kg/m<sup>3</sup>, respectively. Elastic constants used in Figure 2f and Figure 2i can be calculated by rotating  $C_{ij}$  with respect to  $x_2$  axis by 15 and 40 degrees, respectively.

## References

- Ando, M., Y. Ishikawa, F. Yamazaki (1983), Shear wave polarization anisotropy in the upper mantle beneath Honshu, Japan. *J. Geophys. Res.*, *88*, 5850-5864.
- Frederiksen, A. W., and M. G. Bostock (2000), Modeling teleseismic waves in dipping anisotropic structures. *Geophys. J. Int.*, *141*, 401-402
- Long, M., and P. G. Silver (2008), The subduction zone flow field from seismic anisotropy: A global view. *Science*, *319*, 315-318.
- Long, M., and P. G. Silver (2009), Mantle flow in subduction systems: The subslab flow field and implications for mantle dynamics. *J. Geophys. Res.*, *114*, B10312.
- Maggi, A., E. Debayle, K. Priestley, and G. Barruol (2006), Azimuthal anisotropy of the Pacific region. *Earth Planet. Sci. Lett.*, *250*, 53-71.
- Montagner, J.-P., and H.-C. Nataf, (1986), A simple method for inverting the azimuthal anisotropy of surface wave. *J. Geophys. Res.*, *91*, 511-520.
- Smith, D. B., M. H. Ritzwoller, and N. M. Shapiro (2004), Stratification of anisotropy in the Pacific upper mantle. *J. Geophys. Res.*, *109*, B11309.
- Debayle, E., B. Kennet, and K. Priesley (2005), Global azimuthal seismic anisotropy and the unique plate-motion deformation of Australia. *Nature*, *433*, 509-512.
- Song, T.-R. A., and Y.-H. Kim (2012), Anisotropic uppermost mantle in young subducted slab beneath central Mexico. *Nature. Geosci.*, *5*, 55-59.
- Isse, T., H. Shinobara, J.-P., Montagner, H. Sugioka, A. Ito, A. Shito, T. Kanazawa, and K. Yoshizawa (2010), Anisotropic structures of the upper mantle beneath the northern Philippine Sea region from Rayleigh and Love wave tomography. *Phys. Earth Planet. Inter.*, *183*, 33-43.